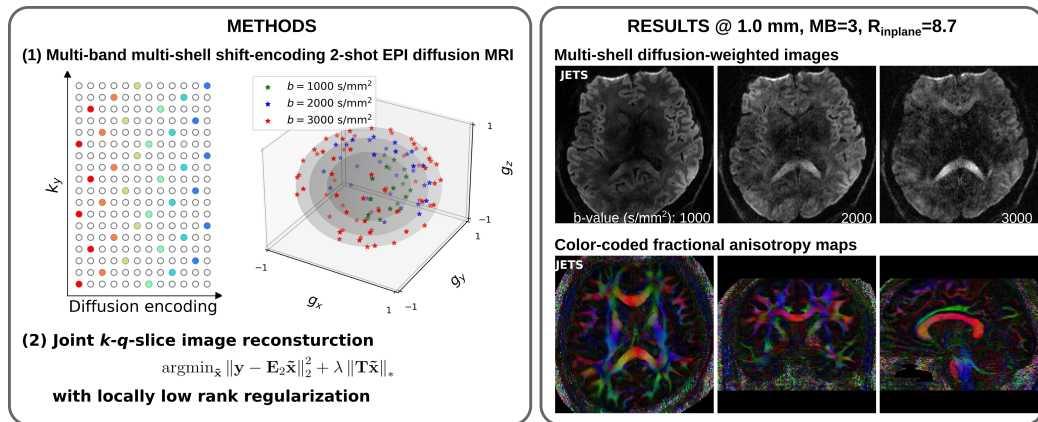


# Graphical Abstract

## Accelerated Diffusion Magnetic Resonance Imaging at 7 T: Joint Reconstruction for Multi-Shell Multi-Band Shift-Encoded Echo Planar Imaging (JETS-EPI)

Zhengguo Tan, Patrick Alexander Liebig, Robin Martin Heidemann, Frederik Bernd Laun, Florian Knoll



## Highlights

### **Accelerated Diffusion Magnetic Resonance Imaging at 7 T: Joint Reconstruction for Multi-Shell Multi-Band Shift-Encoded Echo Planar Imaging (JETS-EPI)**

Zhengguo Tan, Patrick Alexander Liebig, Robin Martin Heidemann, Frederik Bernd Laun, Florian Knoll

- Novel accelerated diffusion acquisition with shifted phase encoding among diffusion directions for complementary  $k$ - $q$ -space sampling at 7 T
- Generalized joint  $k$ - $q$ -slice diffusion-weighted image reconstruction with overlapping locally low-rank regularization
- 5 min 1.2 mm isotropic resolution with  $b$ -value  $1000 \text{ s/mm}^2$  and 32 diffusion directions for in vivo whole-brain diffusion tensor imaging
- 23 min 1 mm isotropic resolution with three-shell high  $b$ -values (up to  $3000 \text{ s/mm}^2$ ) and 126 diffusion directions for in vivo whole-brain diffusion tensor imaging and fiber orientation distribution function (fODF) mapping

# Accelerated Diffusion Magnetic Resonance Imaging at 7 T: Joint Reconstruction for Multi-Shell Multi-Band Shift-Encoded Echo Planar Imaging (JETS-EPI)

Zhengguo Tan<sup>a</sup>, Patrick Alexander Liebig<sup>b</sup>, Robin Martin Heidemann<sup>b</sup>,  
Frederik Bernd Laun<sup>c</sup>, Florian Knoll<sup>a</sup>

<sup>a</sup>*Department Artificial Intelligence in Biomedical Engineering (AIBE),  
Friedrich-Alexander-Universität Erlangen-Nürnberg, Erlangen, Germany*

<sup>b</sup>*Siemens Healthcare GmbH, Erlangen, Germany*

<sup>c</sup>*Institute of Radiology, University Hospital Erlangen, Friedrich-Alexander-Universität  
Erlangen-Nürnberg, Erlangen, Germany*

---

## Abstract

The pursuit of high spatial-angular-temporal resolution for in vivo diffusion-weighted magnetic resonance imaging (DW-MRI) at ultra-high field strength (e.g., 7 T) is important in understanding brain microstructure and function. Such pursuit, however, faces several technical challenges. First, increased off-resonance and shorter  $T_2$  relaxation require faster echo train readouts. Second, high angular resolution in  $q$ -space requires the use of high and/or multiple  $b$ -values, which increases noise in diffusion-weighted images and prolongs scan time. Multi-shot interleaved echo-planar imaging (EPI) and advanced reconstruction strategies, e.g., multiplexed sensitivity-encoding (MUSE) and compressed sensing with structured low-rank matrix completion (MUSSELS), have been proven suitable for high-resolution DW-MRI. These methods, however, do not explore complementary  $k$ - $q$ -space sampling and require longer scan time compared to single-shot EPI. To address these challenges, we developed a novel joint reconstruction for multi-shell multi-

band shift-encoding acquisition at 7 T (JETS-EPI). In comparison to MUSE and MUSSELS, it allows for faster acquisition with the use of high inplane acceleration and only two shots per diffusion direction. Moreover, the proposed joint reconstruction exhibits better denoising of DW images and clearer delineation of fiber distributions.

*Keywords:* Diffusion-weighted magnetic resonance imaging, Echo planar imaging, Ultra high field, Joint reconstruction, Low rank, Simultaneous multi slice

---

<sup>1</sup> **1. Introduction**

<sup>2</sup> Diffusion-weighted magnetic resonance imaging (DW-MRI) ([Le Bihan et al., 1986; Merboldt et al., 1985](#)) is a non-invasive modality that is sen-  
<sup>3</sup> sitive to Brownian motion of water molecules. DW-MRI forms the basis for  
<sup>4</sup> diffusion tensor imaging (DTI) ([Basser et al., 1994; Mori et al., 1999](#)) and  
<sup>5</sup> high angular resolution diffusion imaging (HARDI) ([Tuch et al., 2002](#)), and  
<sup>6</sup> has been widely used in acute brain ischemia diagnosis, in tumor detection  
<sup>7</sup> and staging, and in neuroscience ([Jones, 2010](#)).

<sup>9</sup> For DW-MRI acquisition, the commonly used pulse sequence is single-  
<sup>10</sup> shot echo-planar imaging (SS-EPI) ([Mansfield, 1977](#)). SS-EPI is capable  
<sup>11</sup> of rapidly acquiring one DW image per radio-frequency excitation at the  
<sup>12</sup> order of 100 milliseconds, and is thus motion robust. However, conventional  
<sup>13</sup> SS-EPI, even with three-fold accelerated acquisition ([Bammer et al., 2001](#))  
<sup>14</sup> using parallel imaging ([Roemer et al., 1990; Ra and Rim, 1993; Pruessmann et al., 1999; Griswold et al., 2002](#)), still suffers from low spatial resolution  
<sup>15</sup> and geometric distortions.

<sup>17</sup> In the quest for high-spatial-angular-resolution and minimal-geometry-  
<sup>18</sup> distortion DW-MRI, tremendous efforts have been made. Instead of SS-EPI,  
<sup>19</sup> advanced pulse sequences based on multi-shot EPI have been developed, in-  
<sup>20</sup> cluding but not limited to interleaved EPI ([Butts et al., 1993](#)), PROPELLER  
<sup>21</sup> ([Pipe et al., 2002](#)), readout-segmented EPI ([Porter and Heidemann, 2009; Heidemann et al., 2010](#)), and spiral ([Truong and Guidon, 2014](#)). Multi-shot  
<sup>23</sup> EPI acquisition, however, requires not only longer scan time, but also shot-to-  
<sup>24</sup> shot phase variation correction (due to the use of motion-sensitive diffusion  
<sup>25</sup> gradients).

26 The standard shot-to-shot phase variation correction acquires navigator  
27 echoes at the cost of increased acquisition time. To eliminate this, advanced  
28 self-navigated image reconstruction techniques have been developed. Multi-  
29 plexed sensitivity encoding (MUSE) based on simultaneous-multi-slice (SMS)  
30 (Maudsley, 1980; Breuer et al., 2005) 4-shot interleaved EPI achieved DW-  
31 MRI with sub-millimeter inplane resolution and maximal  $b$ -value  $2000 \text{ s/mm}^2$   
32 at 3 T (Chen et al., 2013). In MUSE, four shots (i.e., four-fold acceleration  
33 per shot) are needed because of two reasons. First, high spatial resolution  
34 requires the use of multi-shot acquisition, which employs shorter echo train  
35 length per shot. This allows for reduced echo time and less spatial distor-  
36 tion. Second, MUSE employs parallel imaging (e.g. SENSE) to reconstruct  
37 shot images for the extraction of shot-to-shot phase variation, and four-fold  
38 acceleration per shot is achievable in parallel imaging.

39 Beyond parallel imaging, compressed sensing opens up the possibility of  
40 higher acceleration in MRI (Lustig et al., 2007; Block et al., 2007). Multi-shot  
41 reconstruction techniques based on structured low-rank matrix completion  
42 (MUSSELS) (Mani et al., 2017; Bilgic et al., 2019) achieved 5-shot DW-  
43 MRI with 9-fold acceleration per shot. Recently, joint usage of structured  
44 low-rank constraints and explicit phase mapping (JULEP) (Dai et al., 2023)  
45 incorporated iterative phase update into MUSSELS using 4-shot DW-MRI  
46 with 4-fold acceleration per shot. All these techniques target the recon-  
47 struction of one DW image from interleaved EPI using at least 4 shots, i.e.,  
48 joint- $k$ - $q$ -space acceleration is not explored.

49 Joint- $k$ - $q$ -space acceleration can be achieved via proper regularization  
50 along the diffusion encoding direction. Relevant examples are diffusion ac-

celeration with Gaussian process estimated reconstruction (DAGER) (Wu et al., 2019) and magnitude-based spatial-angular locally low-rank regularization (SPA-LLR) (Hu et al., 2020). DAGER and SPA-LLR address the reconstruction problem of single-shell diffusion data with  $b$ -values of 1000 and 2000 s/mm<sup>2</sup>, respectively. However, DAGER requires many diffusion directions, whereas SPA-LLR employs the standard interleaved EPI acquisition (i.e., all DW acquisition shares the same inplane sampling pattern). Consequently, these techniques still require long acquisition time.

In this work, we propose a Joint  $k$ - $q$ -slice rEconsTruction framework for multi-band multi-shell Shift-encoded EPI at 7T (dubbed as JETS-EPI). First, our acquisition method differs from most existing techniques as it shifts the  $k$ -space in-plane sampling pattern along the phase encoding ( $k_y$ ) direction. This shifting creates complementary  $k$ - $q$ -space sampling. Second, our reconstruction framework generalizes to jointly reconstruct multi-slice multi-shell multi-direction DW images. This is built upon comprehensive modeling of the acquisition process and construction of regularization terms (e.g. LLR) as proximal operators. We compared our proposed method with state-of-the-art multi-shot reconstruction techniques, i.e., MUSE and MUS-SELS, as well as the established DW image denoising algorithm, i.e., local PCA (Manjón et al., 2013; Veraart et al., 2016). Our proposed method achieves 7T three-shell high  $b$ -value (up to 3000 s/mm<sup>2</sup>) and 126 diffusion direction measurements at 1 mm isotropic resolution in less than 23 min.

<sup>73</sup> **2. Material and methods**

<sup>74</sup> *2.1. Multi-band multi-shell shift-encoded EPI acquisition*

<sup>75</sup> Fig. 1 (A) displays diffusion weighted image acquisition based on two-  
<sup>76</sup> shot interleaved EPI. Conventionally, such a sampling pattern is repeated  
<sup>77</sup> for all diffusion directions. In contrast, we propose the  $k_y$ -shifted diffusion  
<sup>78</sup> encoding, as shown in Fig. 1 (B). The interleaved EPI sampling pattern is  
<sup>79</sup> shifted by one  $k_y$  line per diffusion direction, with the cycling period being  
<sup>80</sup> the in-plane acceleration factor. Fig. 1 (C) displays the employed multi-shell  
<sup>81</sup> sampling pattern. Every diffusion direction is distinct from others, thereby  
<sup>82</sup> constructing a non-colinear sampling pattern. This  $k_y$ -shifted non-colinear  
<sup>83</sup> diffusion encoding exploits complementary  $k$ - $q$ -space sampling. Its benefits  
<sup>84</sup> are two-fold. First, the  $k_y$ -shifting is linear and retains consistent echo spac-  
<sup>85</sup> ing. Second, DW images share anatomical structures but differ in image  
<sup>86</sup> contrast depending on  $b$ -values and diffusion directions, thus complementary  
<sup>87</sup>  $q$ -space sampling is well suited for the exploration of structural similarity.

<sup>88</sup> *2.2. In vivo acquisition protocols*

<sup>89</sup> We implemented multiple in-vivo acquisition protocols at a clinical 7 T  
<sup>90</sup> MR system (MAGNETOM Terra, Siemens Healthineers, Erlangen, Ger-  
<sup>91</sup> many) equipped with a 32-channel head coil (Nova Medical, Wilmington,  
<sup>92</sup> MA, USA) and the XR-gradient system (80 mT/m @ 200 T/m/s). To cali-  
<sup>93</sup> brate coil sensitivity maps, reference scans employed a gradient-echo (GRE)  
<sup>94</sup> sequence. Spectral fat saturation and mono-polar diffusion-encoding gradi-  
<sup>95</sup> ents were used. The phase-encoding direction was selected as anterior-to-  
<sup>96</sup> posterior.

97 This study was approved by the local ethics committee, and informed con-  
98 sent was obtained before scanning healthy volunteers. Detailed acquisition  
99 parameters are listed below.

100 *2.2.1. Single-shell diffusion acquisition at 1.2 mm isotropic resolution*

101 This protocol employed 220 mm FOV in both read and phase-encoding di-  
102 rections, base resolution 182, 94 slices, bandwidth 1832 Hz/Pixel, echo spac-  
103 ing 0.75 ms, TE 47 ms, TR 4300 ms, 2 shots per diffusion direction, in-plane  
104 acceleration 3 as well as partial Fourier 6/8 along the phase-encoding di-  
105 rection, and multi-band factor 2. This results in  $8.7 \times 2$  fold acceleration  
106 per shot. 30 diffusion directions with  $b$ -value 1000 s/mm<sup>2</sup> and 2 diffusion  
107 directions with  $b$ -value 50 s/mm<sup>2</sup> were acquired at a total scan time of 5'3".  
108 Given the high spatial resolution and the short scan time, this protocol fits  
109 well into clinical studies.

110 *2.2.2. Three-shell diffusion acquisition at 1 mm isotropic resolution*

111 This protocol employed the same FOV, shots, inplane acceleration, and  
112 partial Fourier as Section 2.2.1. Other parameters were base resolution 214,  
113 114 slices, bandwidth 1460 Hz/Pixel, echo spacing 0.81 ms, TE 66 ms, TR  
114 5200 ms, and multi-band factor 3. This results in  $8.7 \times 3$  fold acceleration  
115 per shot. As shown in Fig. 1 (C), three shells were sampled (1st shell: 20 dif-  
116 fusion directions with  $b$ -value 1000 s/mm<sup>2</sup>, 2nd shell: 30 diffusion directions  
117 with  $b$ -value 2000 s/mm<sup>2</sup>, and 3rd shell: 64 diffusion directions with  $b$ -value  
118 3000 s/mm<sup>2</sup>).  $b_0$  acquisition was interspersed every ten diffusion directions.  
119 This corresponds to a total of 126 DW acquisition and 22'25" scan time.  
120 This protocol demonstrates the capabilities of JETS-EPI in achieving high

<sub>121</sub> spatial-angular-temporal resolution.

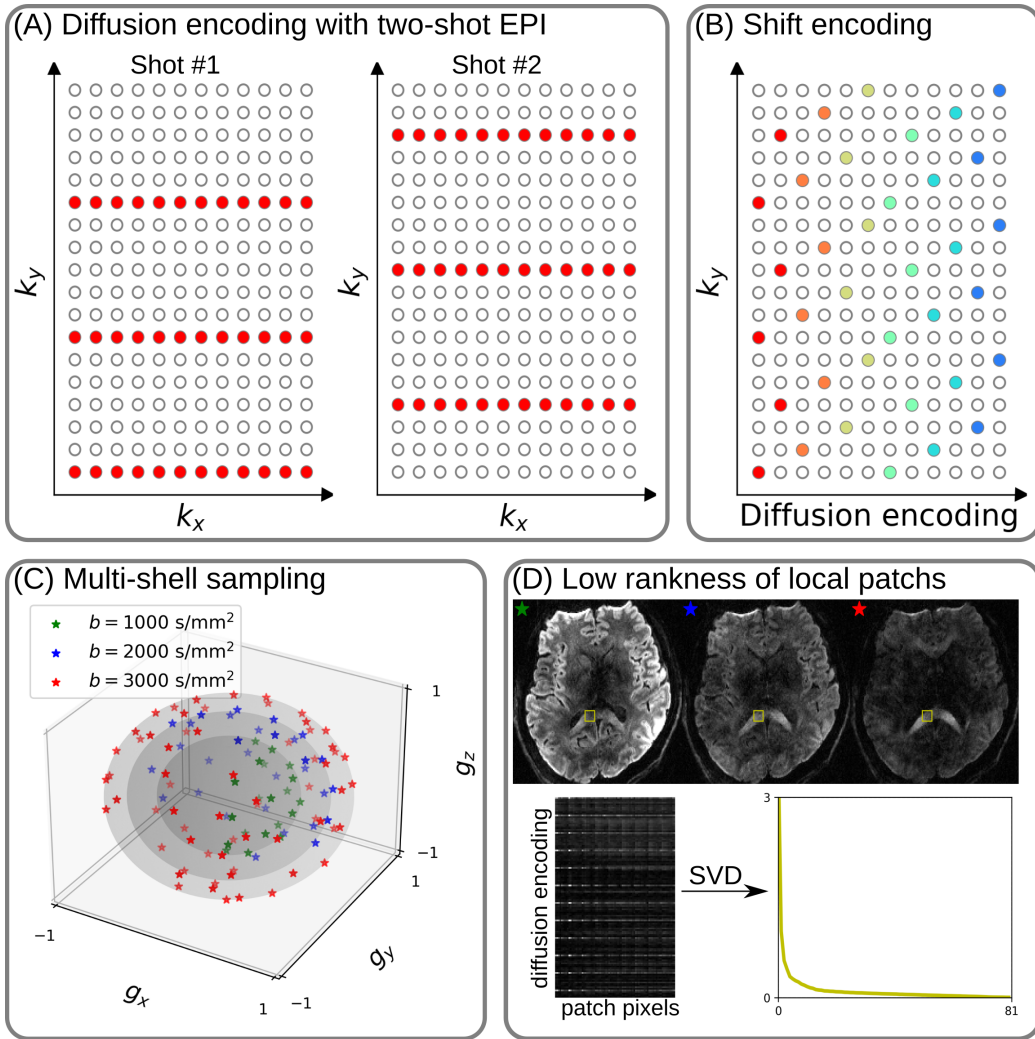


Figure 1: (A) An example DW-MRI acquisition with two-shot interleaved EPI acquisition. (B) The proposed  $k_y$  shifted diffusion encoding scheme. This example employs two shots per DW image. Therefore, every two columns have the same color. (C) An example multi-shell sampling scheme. (D) Low rankness of local image patches (as extracted from the yellow blocks) along multi-shell diffusion encoding.

122    2.3. Forward modeling

123    Our proposed acquisition method yields multi-dimensional but slice col-  
124    lapsed  $k$ -space data  $\mathbf{y}_{c,q,s}$ , where  $c, q, s$  denotes the index of the coil sensitivity  
125    map, the diffusion encoding, and the shot, respectively. Such acquisition can  
126    be modeled in two ways.

First, the acquired  $k$ -space data  $\mathbf{y}$  is mapped from individual shot images  $\mathbf{x}_{q,s,z}$  via the forward model,

$$\mathbf{y}_{c,q,s} = \mathbf{P}_{q,s} \boldsymbol{\Sigma} \boldsymbol{\Theta}_z \mathbf{F} \mathbf{S}_c \mathbf{x}_{q,s,z} \quad (1)$$

$$\mathbf{y} := \mathbf{E}_1 \mathbf{x} \quad (2)$$

127    Here, the encoding matrix  $\mathbf{E}_1$  comprises a chain of linear operators. Every  
128    shot image  $\mathbf{x}$  is point-wise multiplied by a set of coil sensitivity maps ( $\mathbf{S}$ ) and  
129    Fourier transformed ( $\mathbf{F}$ ). The output is then point-wise multiplied by the  
130    multi-slice phase map ( $\boldsymbol{\Theta}$ ) with  $z$  the slice index in simultaneously excited  
131    slices. This operator shifts individual slice along the phase-encoding direction  
132    via varying phase modulation (Breuer et al., 2005). The SMS  $k$ -space data  
133    is then summed (collapsed,  $\boldsymbol{\Sigma}$ ) along the slice dimension and masked (point-  
134    wise multiplied,  $\mathbf{P}$ ) by the sampling pattern at every diffusion encoding and  
135    shot.

136    Second, for diffusion MRI based on multi-shot EPI, shot images per dif-  
137    fusion encoding need to be combined as one DW image ( $\tilde{\mathbf{x}}$ ). One method is  
138    to perform magnitude average (Chen et al., 2013) or root-sum-squares (RSS)  
139    (Mani et al., 2017) of shot images. This method is robust to motion, but  
140    sub-optimal with respect to signal-to-noise ratio (SNR) (Guhaniyogi et al.,  
141    2016). Alternatively, shot combination is done via shot-to-shot phase vari-  
142    ation correction (Liu et al., 2005; Chen et al., 2013). This method can be

<sub>143</sub> written as point-wise multiplication between the shot-to-shot phase variation  
<sub>144</sub> ( $\Phi$ ) and the DW image ( $\tilde{\mathbf{x}}$ ),

$$\mathbf{x}_{q,s,z} = \Phi_{q,s,z} \tilde{\mathbf{x}}_{q,z} \quad (3)$$

<sub>145</sub> Note that  $\tilde{\mathbf{x}}$  can be obtained by applying the adjoint of  $\Phi$  to  $\mathbf{x}$ . In MUSE,  
<sub>146</sub>  $\Phi$  is obtained by parallel imaging reconstruction of all shots with subsequent  
<sub>147</sub> phase smoothing of every shot image (e.g. Hanning window). Based on this  
<sub>148</sub> phase correction method, the complete forward model follows

$$\mathbf{y} := \mathbf{E}_2 \tilde{\mathbf{x}} = \mathbf{E}_1 \Phi \tilde{\mathbf{x}} \quad (4)$$

<sub>149</sub> where the encoding matrix  $\mathbf{E}_2$  comprises the chain of the shot-to-shot phase  
<sub>150</sub> variation  $\Phi$  and the encoding matrix  $\mathbf{E}_1$ .

<sub>151</sub> We implemented these two encoding matrices in SigPy ([Ong and Lustig, 2019](#)), utilizing the concept of object-oriented linear operator abstraction.

#### <sub>153</sub> 2.4. Joint $k$ - $q$ -slice reconstruction

<sub>154</sub> Based on the generalized forward models in Eqs. (2) and (4), our proposed  
<sub>155</sub> joint  $k$ - $q$ -slice reconstruction can be formulated as a three-step approach.

<sub>156</sub> I. Joint reconstruction of all shot images by solving the following inverse  
<sub>157</sub> problem with the LLR regularization:

$$\operatorname{argmin}_{\mathbf{x}} \|\mathbf{y} - \mathbf{E}_1 \mathbf{x}\|_2^2 + \lambda \|\mathbf{T} \mathbf{x}\|_* \quad (5)$$

<sub>158</sub> Note that this step suffices in the case of single-shot EPI acquisition.

<sub>159</sub> II. For multi-shot EPI acquisition, shot-to-shot phase variation is extracted  
<sub>160</sub> from  $\mathbf{x}$ . As phase images are spatially smooth ([Chen et al., 2013; Dai](#)

161 et al., 2023), only the central quarter  $k$ -space region of  $\mathbf{y}$  is used to solve  
162 for  $\mathbf{x}$ . Afterward, the reconstructed  $\mathbf{x}$  is interpolated to the full FOV.  
163 The corresponding phase is then filtered by the Hanning window.

164 III. Joint reconstruction of all DW images using the shot-combined forward  
165 model  $\mathbf{E}_2$  with shot-to-shot phase variation from Step II:

$$\operatorname{argmin}_{\tilde{\mathbf{x}}} \|\mathbf{y} - \mathbf{E}_2 \tilde{\mathbf{x}}\|_2^2 + \lambda \|\mathbf{T} \tilde{\mathbf{x}}\|_* \quad (6)$$

166 2.5. Locally low rank (LLR) regularization

167 As shown in Fig. 1 (D), low rankness exists in local patches from multi-  
168 shell DW images. Intuitively, low rankness comes from the contrast variation  
169 feature of DW images. This motivates the application of LLR regularization  
170 (Trzasko and Manduca, 2011; Zhang et al., 2015) for solving the inverse  
171 problems in Eqs. (5) and (6). Here,  $\lambda$  is the regularization strength ( $\lambda \geq 0$ ).  
172  $\mathbf{T}$  represents a linear operator that firstly slides a local patch window through  
173 all DW images and then flattens every set of local patches to two-dimensional  
174 (2D) matrices. The nuclear norm regularization is enforced via singular value  
175 thresholding of all flattened 2D matrices (Cai et al., 2010). We implemented  
176 this regularization term as an proximal operator (Beck, 2017).

177 Noteworthy, it has been reported that LLR is prone to checkerboard  
178 artifacts when  $\lambda$  is too large (Hu et al., 2020). We overcome this problem  
179 utilizing overlapping blocks and provide an efficient implementation. If the  
180 blocks overlap,  $\mathbf{T}^H \mathbf{T}$  input  $\neq$  input, where  $\mathbf{T}^H$  denotes the adjoint operator  
181 of  $\mathbf{T}$ . Our efficient implementation is to scale  $\mathbf{T}^H$  as  $(1/\text{divisor})\mathbf{T}^H$ , where  
182 the divisor matrix is obtained by  $\mathbf{T}^H \mathbf{T} \mathbf{1}$ .  $\mathbf{1}$  denotes the matrix of ones with  
183 the same shape as input.

184    2.6. Reconstruction

185    The acquired raw data was read in by twixtools (<https://github.com/pehses/twixtools>). Ramp-sampling regridding and FOV/2-ghost correction were also performed in twixtools. Subsequently, coil sensitivity maps were computed from reference scans using ESPIRiT (Uecker et al., 2014) in SigPy (Ong and Lustig, 2019).

190    With this pre-processing as well as the implemented forward models and  
191    the proximal operator, both inverse problems in Eqs. (5) and (6) were solved  
192    by the alternating direction method of multipliers (ADMM) (Boyd et al.,  
193    2010).

194    ADMM solves the minimization problems in an alternating update scheme,

$$\begin{cases} \mathbf{x}^{(k+1)} := \underset{\mathbf{x}}{\operatorname{argmin}} \| \mathbf{y} - \mathbf{E}(\mathbf{x}) \|^2 + \rho/2 \| \mathbf{T}\mathbf{x} - \mathbf{z}^{(k)} + \mathbf{u}^{(k)} \|_2^2 \\ \mathbf{z}^{(k+1)} := \mathcal{T}_{\lambda/\rho}(\mathbf{T}\mathbf{x}^{(k+1)} + \mathbf{u}^{(k)}) \\ \mathbf{u}^{(k+1)} := \mathbf{u}^{(k)} + \mathbf{T}\mathbf{x}^{(k+1)} - \mathbf{z}^{(k+1)} \end{cases} \quad (7)$$

195    where  $k$  denotes the ADMM iteration.  $\mathbf{z}$  is the auxiliary variable ( $\mathbf{z} = \mathbf{T}\mathbf{x}$ ),  
196    and  $\mathbf{u}$  is the Lagrangian multipliers. Noteworthy, in Eq. (7),  $\mathbf{x}$   $\mathbf{E}$  stand  
197    for shot images and  $\mathbf{E}_1$  when solving Eq. (2), and shot-combined images  
198    and  $\mathbf{E}_2$  when solving Eq. (4), respectively.  $\mathbf{x}$  can be solved using linear least  
199    square algorithms, e.g. conjugate gradient (Hestenes and Stiefel, 1952), while  
200     $\mathbf{z}$  is updated via singular value thresholding. The coupling parameter  $\rho$  is  
201    effective in both the update of  $\mathbf{x}$  and  $\mathbf{z}$ . It acts as Tikhonov regularization  
202    strength when updating  $\mathbf{x}$ , but also inversely scales the thresholding strength  
203    when updating  $\mathbf{z}$ , as shown in Supporting Information Figures S1 and S2.

204    In this work, 15 ADMM iterations with  $\rho = 0.05$  and  $\lambda = 0.04$ , and a  
205    block size of 6 for LLR (refer to Supporting Information Figure S3) were

206 used. All reconstructions were done on a single A100 SXM4/Nvlink GPU  
207 with 40 GB memory (NVIDIA, Santa Clara, CA, USA).

208 We compared our proposed joint reconstruction with established multi-  
209 shot reconstruction techniques, i.e. MUSE (Chen et al., 2013) and MUSSELS  
210 (Mani et al., 2017). We implemented both techniques in Python and vali-  
211 dated them with open-source codes and data (Dai et al., 2023; Bilgic et al.,  
212 2019). For implementation details, please refer to "Reproducing MUSE  
213 and MUSSELS in Python" in the Supporting Information. Further, we de-  
214 noised MUSE diffusion-weighted images with local PCA (Manjón et al., 2013;  
215 Veraart et al., 2016).

216 With reconstructed DW images, fractional anisotropy (FA) maps (Basser  
217 et al., 1994) were fitted using our implementation in Python, whereas fiber  
218 orientation distribution functions (fODF) (Aganj et al., 2009) were computed  
219 in MITK-Diffusion (Fritzsche et al., 2012) with the spherical harmonic order  
220 4 and the regularization factor 0.002. fODF maps were displayed with the  
221 min-max normalization and the FA/GFA scaling factor 2.2.

222 **3. Results**

223 *3.1. Single-shell diffusion acquisition at 1.2 mm isotropic resolution*

224 Fig. 2 displays a DW image for one diffusion direction and zoomed-in  
225 colored FA maps from MUSE, MUSE with denoising, MUSSELS, and JETS  
226 reconstruction. Both MUSE and MUSSELS exhibit residual noise artifacts  
227 for the single-shell acquisition with the  $b$ -value of 1000 s/mm<sup>2</sup>. The local PCA  
228 denoiser removes noise, but the denoised DW image loses fine structures,  
229 e.g. the cuneus (highlighted by the arrows in the figure). This over-smoothing  
230 effect can also be observed in the colored FA map, where the thin fibers near  
231 to gray matter are missing.

232 *3.2. Three-shell diffusion acquisition at 1.0 mm isotropic resolution*

233 Results for a 1.0 mm isotropic resolution three-shell 126-direction diffusion  
234 acquisition are shown in Fig. 3. At this resolution severe reduction of signal-  
235 to-noise ratio (SNR) can be observed for higher  $b$ -values. With such low SNR  
236 levels, brain structures are completely buried below the noise level in MUSE  
237 and MUSSELS. The local PCA denoiser removes noise efficiently from the  
238 reconstructed MUSE images, but images from higher  $b$ -values suffer from  
239 severe blurring that leads to a loss of fine image details. Only the proposed  
240 JETS method with the combination of the  $k_y$ -shift encoding scheme and LLR  
241 regularized reconstruction allows to resolve brain features for higher  $b$ -values.

242 Fig. 4 shows fitted FA maps in three orthogonal orientations based on  
243 the above four DW image reconstruction methods. Corresponding color-  
244 coded FA maps are provided in Supporting Information Figure S6. All FA  
245 maps are displayed with the same windowing, i.e., minimal and maximal

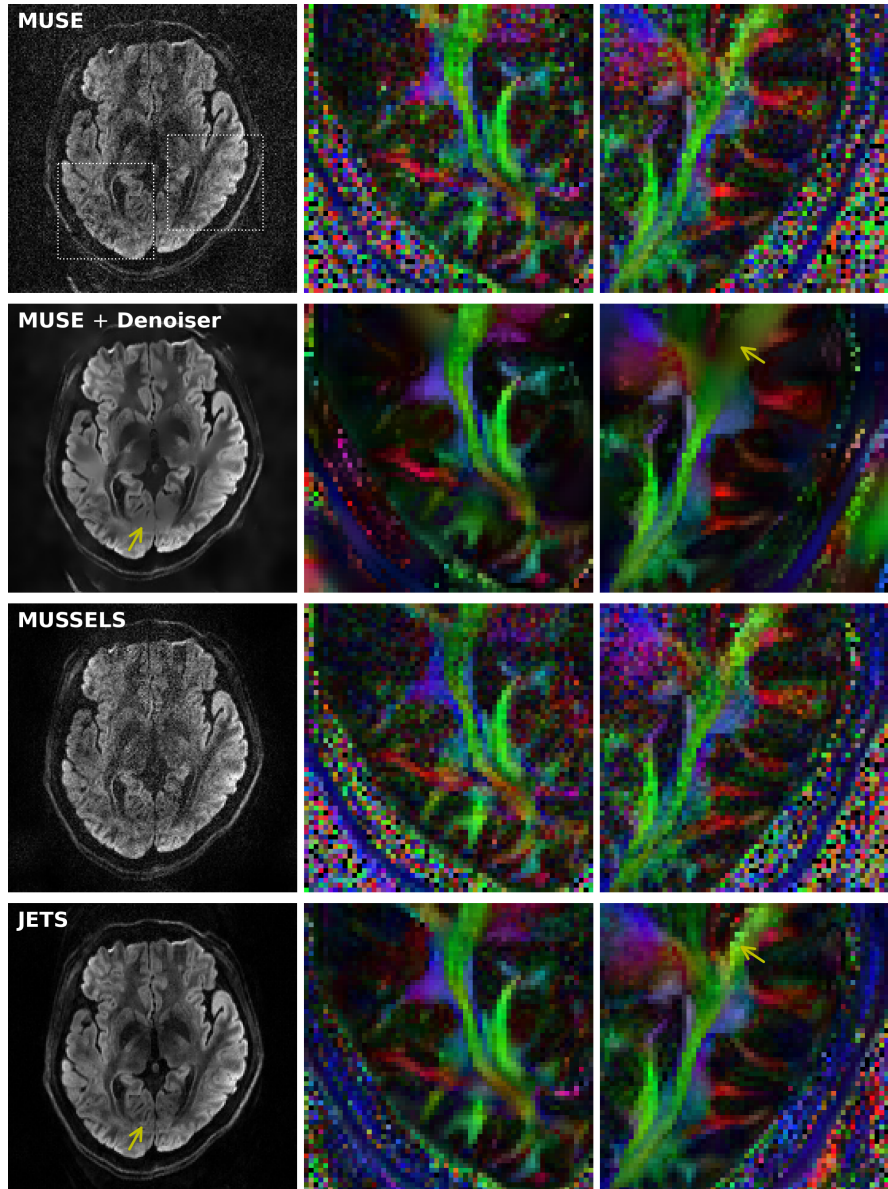


Figure 2: Comparison of reconstructions of a single-shell diffusion acquisition at 1.2 mm isotropic resolution: (1st row) MUSE, (2nd row) MUSE with local PCA denoising, (3rd row) MUSSELS, and (4th row) our proposed JETS approach. The DW image of the 42nd slice and 24th diffusion direction and its zoomed-in colored fractional anisotropy (FA) maps (dashed rectangles) are displayed. The denoiser over-smoothes the images, resulting in missing thin veins and fibers (indicated by yellow arrows).

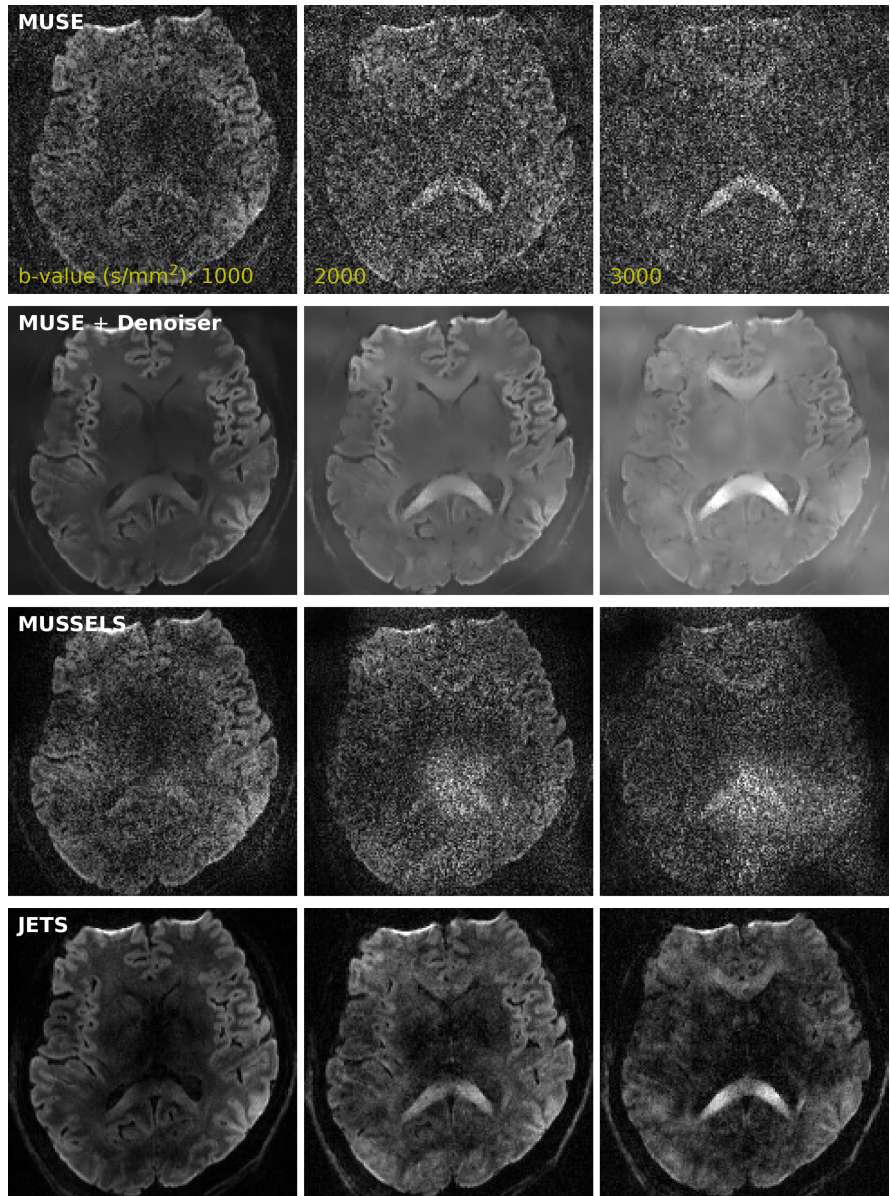


Figure 3: Comparison of reconstructed DW images on three-shell diffusion acquisition at 1 mm isotropic resolution. DW images of the 60th slice for one diffusion direction at different  $b$ -values are displayed: (left) 1000, (center) 2000, and (right) 3000  $\text{s}/\text{mm}^2$ .

values set as 0 and 1, respectively. The FA maps from MUSE with local PCA desnoing exhibit much lower values than other methods. This may be caused by the excessive noise in DW images from MUSE or by the automatic noise estimate in the local PCA denoising algorithm (Veraart et al., 2016). Among all methods, FA maps from JETS show better quality and delineate fine details within the putamen (see white arrows).

Fig. 5 shows fODF maps within the rectangular regions in Fig. 4. This result again demonstrates the advantage of iterative reconstruction with LLR regularization for DW image denoising. Both MUSE and MUSSELS reconstructions suffer from noise artifacts due to the use of highly accelerated acquisition ( $R = 8.7 \times 3$  per shot) and high  $b$ -values (up to  $3000\text{ s/mm}^2$ ). As a result, their corresponding fODF maps illustrate chaotic fiber orientation. With the local PCA denoiser applied to DW images reconstructed by MUSE, the fODF peaks show improved smooth patterns, but the FA values are reduced due to excessive noise in DW images. In contrast, with LLR regularization applied to the spatial-angular patches, JETS is able to resolve crossing fibers in the intersection of corpus callosum and superior longitudinal fasciculus (see white arrows).

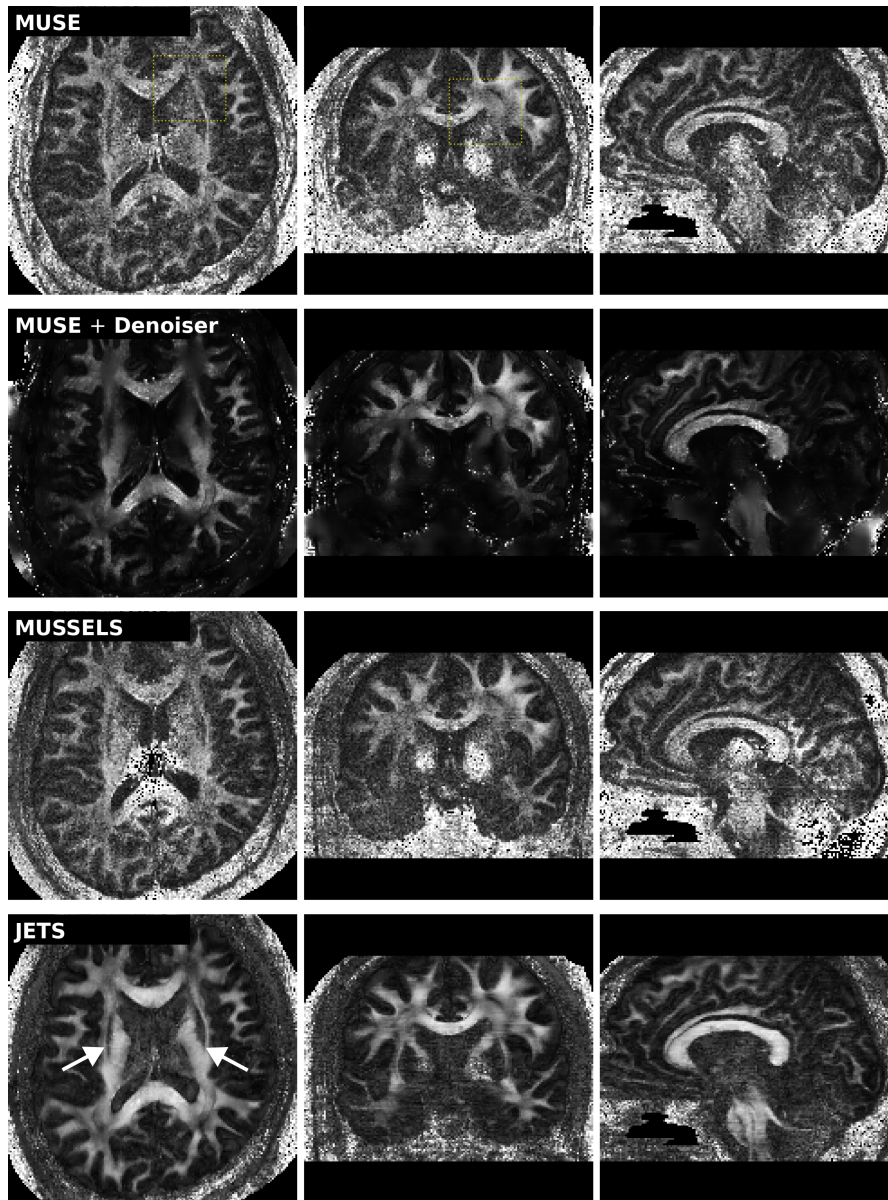


Figure 4: Comparison of reconstructed FA maps based on the 1 mm isotropic resolution three-shell diffusion acquisition. One slice from every orientation (axial, coronal, and sagittal view from left to right) was selected for display.

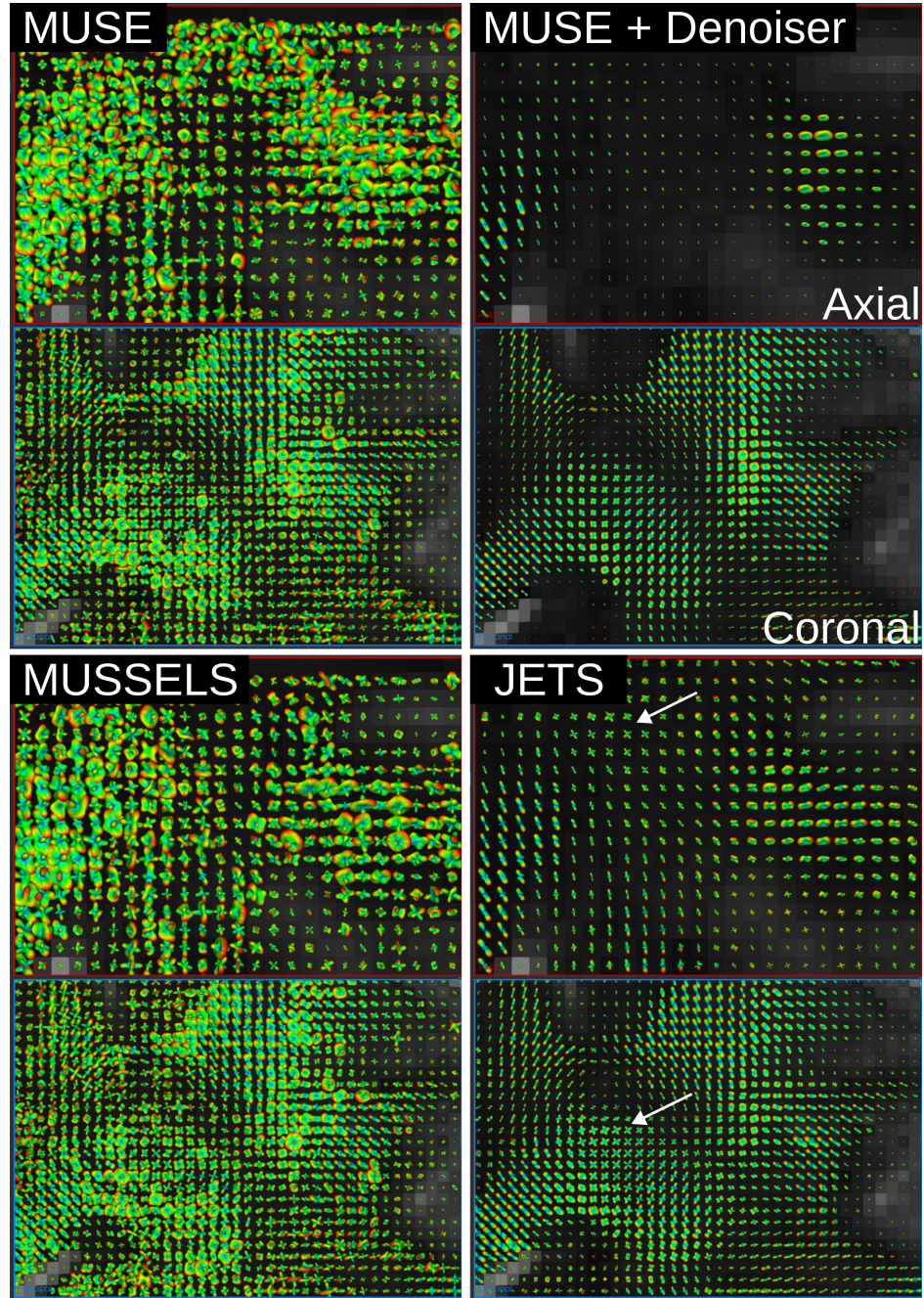


Figure 5: Comparison of fODF peaks within the dashed rectangles of (red) the axial and (blue) the coronal slices in Fig. 4, respectively.

264 **4. Discussion**

265 This work reports a novel DW-MRI technique, dubbed as JETS-EPI,  
266 comprising two ingredients, multi-band  $k_y$ -shift-encoded interleaved EPI for  
267 complementary  $k$ - $q$ -space sampling, and a generalized joint reconstruction  
268 with overlapping locally low-rank regularization to explore low rankness along  
269 the diffusion encoding dimension. JETS-EPI utilizes only two shots per  
270 diffusion direction, thereby allowing for short scan time as well as high spatial  
271 resolution with reduced geometric distortion. Our reconstruction achieves  
272  $8.7 \times 3$  ( $R_{\text{inplane}} \times \text{SMS}$ ) fold accelerated brain DW-MRI at 7 T with 1 mm  
273 isotropic resolution and 126 diffusion-direction (three shells with  $b$ -values of  
274 1000, 2000, and 3000 s/mm<sup>2</sup>) in less than 23 min.

275 The reconstruction results from MUSE and MUSSELS suffer from noise  
276 effects in this study, and the reasons are two-fold. First, the high in-plane  
277 acceleration factor per shot hinders shot-to-shot phase variation estimation  
278 in MUSE, whereas we proposed to jointly reconstruct all shot images from  
279 the central  $k$ -space data. Further, joint reconstruction benefits from the  
280 complementary  $k$ - $q$ -space sampling, as compared to the shot-by-shot parallel  
281 imaging reconstruction. Second, structured low-rank matrix completion as  
282 MUSSELS usually works with at least four shots per diffusion direction,  
283 whereas this study uses only two shots. The use of two shots is beneficial  
284 for shorter scan time than four shots, but hinders the structured low rank  
285 property in MUSSELS.

286 One limitation of JETS-EPI is the long reconstruction time due to the  
287 simultaneous reconstruction of all DW images and the use of overlapping  
288 locally low-rank regularization. The reconstruction of the protocols in Sec-

tion 2.2.1 and Section 2.2.2 on GPU A100 takes about 0.5 h and 3 h per collapsed slice, respectively. To reduce the computation time, coil compression algorithms (Huang et al., 2008) can be employed to reduce the number of coils for image reconstruction. Moreover, one may deploy multi-GPU distributed computing or modern optimization algorithms (e.g. stochastic gradient descent) (Ong et al., 2020) to speed up the reconstruction.

Another limitation of JETS-EPI is the self-navigated shot-to-shot phase variation estimation, which was performed based on the central quarter  $k$ -space region of every shot. These shot  $k$ -space data is highly undersampled with  $R = 8.7 \times 3$  for the 1 mm three-shell diffusion acquisition. Such high acceleration may result in sub-optimal phase estimation, especially in regions with low SNR and/or rapid phase change.

While this work reconstructs all DW images and then performs model fitting, an alternative approach is to directly estimate  $b_0$  and diffusion tensors from measured  $k$ - $q$ -space data using model-based reconstruction (Knoll et al., 2015; Dong et al., 2018; Shafieizargar et al., 2023). Compared to DW image reconstruction, model-based reconstruction solves for fewer number of unknowns, but requires strict diffusion tensor modeling and the use of nonlinear least square solvers.

## 5. Conclusions

We demonstrated the JETS-EPI technique, which integrates a  $k_y$ -shifted encoding interleaved EPI sequence and a joint reconstruction with overlapping locally low-rank regularization for high spatial-angular-temporal resolution DW-MRI at 7 T. This technique requires no phase navigation, and

313 allows for high quality DW image reconstruction with accelerated acquisition.  
314

315 **Funding**

316 This work was supported by Deutsche Forschungsgemeinschaft (DFG) -  
317 Project Number 513220538, as well as National Institutes of Health (NIH)  
318 R01 EB024532 and P41 EB017183.

319 **Data and code available statement**

320 In the spirit of reproducible and open science, we will publish our source  
321 code (<https://github.com/ZhengguoTan/sigpy>) as well as the raw  $k$ -space  
322 data (<https://doi.org/10.5281/zenodo.7548595>) during the review pro-  
323 cess.

324 **Acknowledgments**

325 The authors thank Dr. Peter Neher for discussions. The authors grate-  
326 fully acknowledge the scientific support and HPC resources provided by the  
327 Erlangen National High Performance Computing Center (NHR@FAU) of  
328 Friedrich-Alexander-Universität Erlangen-Nürnberg (FAU) under the NHR  
329 project b143dc. NHR funding is provided by federal and Bavarian state au-  
330 thorities. NHR@FAU hardware is partially funded by the German Research  
331 Foundation (DFG) – 440719683.

332    **References**

- 333    Aganj, I., Lenglet, C., Sapiro, G., 2009. Odf reconstruction in q-ball imaging with solid angle consideration, in: Proc. IEEE Int. Symp. Biomed. Imaging, pp. 1398–1401. doi:[10.1109/ISBI.2009.5193327](https://doi.org/10.1109/ISBI.2009.5193327).
- 336    Bammer, R., Keeling, S.L., Augustin, M., Pruessmann, K.P., Wolf, R., Stoll-  
337    berger, R., Hartung, H.P., Fazekas, F., 2001. Improved diffusion-weighted  
338    single-shot echo-planar imaging (EPI) in stroke using sensitivity encoding  
339    (SENSE). Magn. Reson. Med. 46, 548–554. doi:[10.1002/mrm.1226](https://doi.org/10.1002/mrm.1226).
- 340    Basser, P.J., Mattiello, J., Le Bihan, D., 1994. MR diffusion tensor  
341    spectroscopy and imaging. Biophys. J. 66, 259–267. doi:[10.1016/S0006-3495\(94\)80775-1](https://doi.org/10.1016/S0006-3495(94)80775-1).
- 343    Beck, A., 2017. First-order methods in optimization. Society for In-  
344    dustrial and Applied Mathematics, Philadelphia, PA. doi:[10.1137/1.9781611974997](https://doi.org/10.1137/1.9781611974997).
- 346    Bilgic, B., Chatnuntawech, I., Manhard, M.K., Tian, Q., Liao, C., Iyer, S.S.,  
347    Cauley, S.F., Huang, S.Y., Polimeni, J.R., Wald, L.L., Setsompop, K.,  
348    2019. Highly accelerated multishot echo planar imaging through synergistic  
349    machine learning and joint reconstruction. Magn. Reson. Med. 82, 1343–  
350    1358. doi:[10.1002/mrm.27813](https://doi.org/10.1002/mrm.27813).
- 351    Block, K.T., Uecker, M., Frahm, J., 2007. Undersampled radial MRI with  
352    multiple coils. Iterative image reconstruction using a total variation con-  
353    straint. Magn. Reson. Med. 57, 1186–1098. doi:[10.1002/mrm.21236](https://doi.org/10.1002/mrm.21236).

- 354 Boyd, S., Parikh, N., Chu, E., Peleato, B., Eckstein, J., 2010. Distributed  
355 optimization and statistical learning via the alternating direction method  
356 of multipliers. *Foundations and Trends in Machine Learning* 3, 1–122.  
357 doi:[10.1561/2200000016](https://doi.org/10.1561/2200000016).
- 358 Breuer, F.A., Blaimer, M., Heidemann, R.M., Mueller, M.F., Griswold, M.A.,  
359 Jakob, P.M., 2005. Controlled Aliasing in Parallel Imaging Results in  
360 Higher Acceleration (CAPIRINHA) for Multi-Slice Imaging. *Magn. Reson.*  
361 *Med.* 53, 684–691. doi:[10.1002/mrm.20401](https://doi.org/10.1002/mrm.20401).
- 362 Butts, K., Riederer, S.J., Ehman, R.L., Thompson, R.M., Jack, C.R., 1993.  
363 Interleaved echo planar imaging on a standard MRI system. *Magn. Reson.*  
364 *Med.* 31, 67–72. doi:[10.1002/mrm.1910310111](https://doi.org/10.1002/mrm.1910310111).
- 365 Cai, J.F., Candès, E.J., Shen, Z., 2010. A singular value thresholding  
366 algorithm for matrix completion. *SIAM. J. Optim.* 20, 1956–1982.  
367 doi:[10.1137/080738970](https://doi.org/10.1137/080738970).
- 368 Chen, N.K., Guidon, A., Chang, H.C., Song, A.W., 2013. A robust multi-  
369 shot scan strategy for high-resolution diffusion weighted MRI enabled by  
370 multiplexed sensitivity-encoding (MUSE). *NeuroImage* 72, 41–47. doi:[10.1016/j.neuroimage.2013.01.038](https://doi.org/10.1016/j.neuroimage.2013.01.038).
- 372 Dai, E., Mani, M., McNab, J.A., 2023. Multi-band multi-shot diffu-  
373 sion MRI reconstruction with joint usage of structured low-rank con-  
374 straints and explicit phase mapping. *Magn. Reson. Med.* 89, 95–111.  
375 doi:[10.1002/mrm.29422](https://doi.org/10.1002/mrm.29422).

- 376 Dong, Z., Dai, E., Wang, F., Zhang, Z., Ma, X., Yuan, C., Guo, H., 2018.  
377 Model-based reconstruction for simultaneous multislice and parallel imag-  
378 ing accelerated multishot diffusion tensor imaging. *Med. Phys.* 45, 3196–  
379 3204. doi:[10.1002/mp.12974](https://doi.org/10.1002/mp.12974).
- 380 Fritzzsche, K.H., Neher, P.F., Reicht, I., van Bruggen, T., Goch, C., Reisert,  
381 M., Nolden, M., Zelzer, S., Meinzer, H.P., Stieltjes, B., 2012. MITK diffu-  
382 sion imaging. *Methods Inf. Med.* 51, 441–448. doi:[10.3414/ME11-02-0031](https://doi.org/10.3414/ME11-02-0031).
- 383 Griswold, M.A., Jakob, P.M., Heidemann, R.M., Nittka, M., Jellus, V.,  
384 Wang, J., Kiefer, B., Haase, A., 2002. Generalized autocalibrating par-  
385 tially parallel acquisitions (GRAPPA). *Magn. Reson. Med.* 47, 1202–1210.  
386 doi:[10.1002/mrm.10171](https://doi.org/10.1002/mrm.10171).
- 387 Guhaniyogi, S., Chu, M.L., Chang, H.C., Song, A.W., Chen, N.K., 2016. Mo-  
388 tion immune diffusion imaging using augmented MUSE for high-resolution  
389 multi-shot EPI. *Magn. Reson. Med.* 75, 639–652. doi:[10.1002/mrm.25624](https://doi.org/10.1002/mrm.25624).
- 390 Heidemann, R.M., Porter, D.A., Anwander, A., Feiweier, T., Heberlein, K.,  
391 Knösche, T.R., Turner, R., 2010. Diffusion imaging in humans at 7 T  
392 using readout-segmented EPI and GRAPPA. *Magn. Reson. Med.* 64, 9–  
393 14. doi:[10.1002/mrm.22480](https://doi.org/10.1002/mrm.22480).
- 394 Hestenes, M.R., Stiefel, E., 1952. Methods of conjugate gradients for solving  
395 linear systems. *J. Res. Natl. Bur. Stand.* 49, 409–436. doi:[10.6028/jres.049.044](https://doi.org/10.6028/jres.049.044).
- 397 Hu, Y., Wang, X., Tian, Q., Yang, G., Daniel, B., McNab, J., Hargreaves, B.,  
398 2020. Multi-shot diffusion-weighted MRI reconstruction with magnitude-

- 399 based spatial-angular locally low-rank regularization (SPA-LLR). Magn.  
400 Reson. Med. 83, 1596–1607. doi:[10.1002/mrm.28025](https://doi.org/10.1002/mrm.28025).
- 401 Huang, F., Vijayakumar, S., Li, Y., Hertel, S., Duensing, G.R., 2008. A soft-  
402 ware channel compression technique for faster reconstruction with many  
403 channels. Magn. Reson. Imaging 26, 133–141.
- 404 Jones, D.K., 2010. Diffusion MRI: Theory, methods, and applications. Oxford  
405 University Press.
- 406 Knoll, F., Raya, J.G., Halloran, R.O., Baete, S., Sigmund, E., Bammer, R.,  
407 Block, T., Otazo, R., Sodickson, D.K., 2015. A model-based reconstruction  
408 for undersampled radial spin-echo DTI with variational penalties on the  
409 diffusion tensor. NMR Biomed 28, 353–366.
- 410 Le Bihan, D., Breton, E., Lallemand, D., Grenier, P., Cabanis, E., Laval-  
411 Jeantet, M., 1986. MR imaging of intravoxel incoherent motions: appli-  
412 cation to diffusion and perfusion in neurologic disorders. Radiology 161,  
413 401–407. doi:[10.1148/radiology.161.2.3763909](https://doi.org/10.1148/radiology.161.2.3763909).
- 414 Liu, C., Moseley, M.E., Bammer, R., 2005. Simultaneous phase cor-  
415 rection and SENSE reconstruction for navigated multi-shot DWI with  
416 non-Cartesian  $k$ -space sampling. Magn. Reson. Med. 54, 1412–1422.  
417 doi:[10.1002/mrm.20706](https://doi.org/10.1002/mrm.20706).
- 418 Lustig, M., Donoho, D., Pauly, J.M., 2007. Sparse MRI: The application of  
419 compressed sensing for rapid MR imaging. Magn. Reson. Med. 58, 1182–  
420 1195. doi:[10.1002/mrm.21391](https://doi.org/10.1002/mrm.21391).

- 421 Mani, M., Jacob, M., Kelley, D., Magnotta, V., 2017. Multi-shot sensitivity-  
422 encoded diffusion data recovery using structured low-rank matrix comple-  
423 tion (MUSSELS). *Magn. Reson. Med.* 78, 494–507. doi:[10.1002/mrm.26382](https://doi.org/10.1002/mrm.26382).
- 425 Manjón, J.V., Coupé, P., Concha, L., Buades, A., Collins, D.L., Robles, M.,  
426 2013. Diffusion weighted image denoising using overcomplete local PCA.  
427 *PLoS One* 8, e73021. doi:[10.1371/journal.pone.0073021](https://doi.org/10.1371/journal.pone.0073021).
- 428 Mansfield, P., 1977. Multi-planar image formation using NMR spin echoes.  
429 *J Phys C* 10, 55–58. doi:[10.1088/0022-3719/10/3/004](https://doi.org/10.1088/0022-3719/10/3/004).
- 430 Maudsley, A.A., 1980. Multiple-line-scanning spin density imaging. *J. Magn.*  
431 *Reson.* 41, 112–126. doi:[10.1016/0022-2364\(80\)90207-3](https://doi.org/10.1016/0022-2364(80)90207-3).
- 432 Merboldt, K.D., Hanicke, W., Frahm, J., 1985. Self-diffusion NMR imag-  
433 ing using stimulated echoes. *J. Magn. Reson.* 64, 479–486. doi:[10.1016/0022-2364\(85\)90111-8](https://doi.org/10.1016/0022-2364(85)90111-8).
- 435 Mori, S., Crain, B.J., Chacko, V.P., Van Zijl, P.C.M., 1999. Three-  
436 dimensional tracking of axonal projections in the brain by mag-  
437 netic resonance imaging. *Ann. Neurol.* 45, 265–269. doi:[10.1002/1531-8249\(199902\)45:2<265::AID-ANA21>3.0.CO;2-3](https://doi.org/10.1002/1531-8249(199902)45:2<265::AID-ANA21>3.0.CO;2-3).
- 439 Ong, F., Lustig, M., 2019. SigPy: A Python package for high performance  
440 iterative reconstruction, in: Proceedings of the 27th Annual Meeting of  
441 ISMRM, Montréal, CAN, p. 4819.
- 442 Ong, F., Zhu, X., Cheng, J.Y., Johnson, K.M., Larson, P.E.Z., Vasanawala,  
443 S.S., Lustig, M., 2020. Extreme MRI: Large-scale volumetric dynamic

- 444 imaging from continuous non-gated acquisitions. Magn. Reson. Med. 84,  
445 1763–1780. doi:[10.1002/mrm.28235](https://doi.org/10.1002/mrm.28235).
- 446 Pipe, J.G., Farthing, V.G., Forbes, K.P., 2002. Multishot diffusion-weighted  
447 FSE using PROPELLER MRI. Magn. Reson. Med. 47, 42–52. doi:[10.1002/mrm.10014](https://doi.org/10.1002/mrm.10014).
- 449 Porter, D.A., Heidemann, R.M., 2009. High resolution diffusion-weighted  
450 imaging using readout-segmented echo-planar imaging, parallel imaging  
451 and a two-dimensional navigator-based reacquisition. Magn. Reson. Med.  
452 62, 468–475. doi:[10.1002/mrm.22024](https://doi.org/10.1002/mrm.22024).
- 453 Pruessmann, K.P., Weiger, M., Scheidegger, M.B., Boesiger, P., 1999.  
454 SENSE: Sensitivity encoding for fast MRI. Magn. Reson. Med. 42, 952–  
455 962. doi:[10.1002/\(SICI\)1522-2594\(199911\)42:5<952::AID-MRM16>3.0.CO;2-S](https://doi.org/10.1002/(SICI)1522-2594(199911)42:5<952::AID-MRM16>3.0.CO;2-S).
- 457 Ra, J.B., Rim, C.Y., 1993. Fast imaging using subencoding data sets from  
458 multiple detectors. Magn. Reson. Med. 30, 142–145. doi:[10.1002/mrm.1910300123](https://doi.org/10.1002/mrm.1910300123).
- 460 Roemer, P.B., Edelstein, W.A., Hayes, C.E., Souza, S.P., Mueller, O.M.,  
461 1990. The NMR phased array. Magn. Reson. Med. 16, 192–225. doi:[10.1002/mrm.1910160203](https://doi.org/10.1002/mrm.1910160203).
- 463 Shafieizargar, B., Jeurissen, B., Poot, D.H.J., Klein, S., Van Audekerke,  
464 J., Verhoye, M., den Dekker, A.J., Sijbers, J., 2023. ADEPT: Accurate  
465 diffusion echo-planar imaging with multi-contrast sh0Ts. Magn. Reson.  
466 Med. 89, 396–410. doi:[10.1002/mrm.29398](https://doi.org/10.1002/mrm.29398).

- <sup>467</sup> Truong, T.K., Guidon, A., 2014. High-resolution multishot spiral diffusion  
<sup>468</sup> tensor imaging with inherent correction of motion-induced phase errors.  
<sup>469</sup> Magn. Reson. Med. 71, 790–796. doi:[10.1002/mrm.24709](https://doi.org/10.1002/mrm.24709).
- <sup>470</sup> Trzasko, J., Manduca, A., 2011. Local versus global low-rank promotion in  
<sup>471</sup> dynamic MRI series reconstruction, in: Proceedings of the 19th Annual  
<sup>472</sup> Meeting of ISMRM, Montréal, CAN, p. 4371.
- <sup>473</sup> Tuch, D.S., Reese, T.G., Wiegell, M.R., Makris, N., Belliveau, J.W., Wedeen,  
<sup>474</sup> V.J., 2002. High angular resolution diffusion imaging reveals intravoxel  
<sup>475</sup> white matter fiber heterogeneity. Magn. Reson. Med. 48, 577–582. doi:[10.1002/mrm.10268](https://doi.org/10.1002/mrm.10268).
- <sup>477</sup> Uecker, M., Lai, P., Murphy, M.J., Virtue, P., Elad, M., Pauly, J.M.,  
<sup>478</sup> Vasanawala, S.S., Lustig, M., 2014. ESPIRiT – an eigenvalue approach  
<sup>479</sup> to autocalibrating parallel MRI: Where SENSE meets GRAPPA. Magn.  
<sup>480</sup> Reson. Med. 71, 990–1001. doi:[10.1002/mrm.24751](https://doi.org/10.1002/mrm.24751).
- <sup>481</sup> Veraart, J., Novikov, D.S., Christiaens, D., Ades-aron, B., Sijbers, J., Fiere-  
<sup>482</sup> mans, E., 2016. Denoising of diffusion mri using random matrix theory.  
<sup>483</sup> NeuroImage 142, 394–406. doi:[10.1016/j.neuroimage.2016.08.016](https://doi.org/10.1016/j.neuroimage.2016.08.016).
- <sup>484</sup> Wu, W., Koopmans, P.J., Andersson, J.L., Miller, K.L., 2019. Diffusion  
<sup>485</sup> Acceleration with Gaussian process Estimated Reconstruction (DAGER).  
<sup>486</sup> Magn. Reson. Med. 82, 107–125. doi:[10.1002/mrm.27699](https://doi.org/10.1002/mrm.27699).
- <sup>487</sup> Zhang, T., Pauly, J.M., Levesque, I.R., 2015. Accelerated parameter mapping  
<sup>488</sup> with a locally low rank constraint. Magn. Reson. Med. 73, 655–661. doi:[10.1002/mrm.25161](https://doi.org/10.1002/mrm.25161).